Available online at www.sciencedirect.com
SCIENCE DIRECT®
Computer Physics Communications 158 (2004) 47–56
Computer Physics Communications
www.elsevier.com/locate/cpc

Three-dimensional MHD high-resolution computations with CWENO employing adaptive mesh refinement

Jens Kleimann [a,*], Andreas Kopp [a], Horst Fichtner [a], Rainer Grauer [b], Kai Germaschewski [b]

[a] *Institut für Theoretische Physik, Lehrstuhl IV, Ruhr-Universität Bochum, 44780 Bochum, Germany*
[b] *Institut für Theoretische Physik, Lehrstuhl I, Ruhr-Universität Bochum, 44780 Bochum, Germany*

Received 22 April 2003; received in revised form 28 November 2003; accepted 9 December 2003

Abstract

Until recently, numerical simulations of discontinuities in highly super-Alfvénic plasmas have been severely limited by comparatively crude resolution and accuracy. Significant progress in the numerical simulation of such plasmas was achieved with the recently implemented *Central Weighted Essentially Non-Oscillatory* (CWENO) scheme. Combining this technique with that of adaptive mesh refinement (AMR), we have developed a third-order numerical scheme, which is able to efficiently capture strong gradients on spatial scales being small compared to the overall scale of the plasma system considered. Here, we first describe important algorithmic aspects of the scheme as well as the physics included in it. Second, we present the results of various performance tests. And, third, we illustrate its application to 'real world problems' using the example of the dynamics of a Sedov-type explosion.

Keywords: Multi-dimensional MHD simulation; Central weighted essentially non-oscillatory scheme; Adaptive mesh refinement

1. Motivation

The motivation for developing a new numerical scheme was two-fold. First, a correct and insightful treatment of various plasma systems in both laboratory and space plasmas requires the resolution of scales being very small compared to the extent of the entire system. In laboratory plasmas typical small scale problems occur in the context of fast reconnection (Biskamp [1]) in the sawtooth crash, where the dynamics on the macroscale (several meters) is determined by instabilities and turbulence on the electron skin depth (∼0.05 cm). In space plasmas the situation is similar. Plasma contact or tangential discontinuities as well as shocks can be as narrow as the electron inertial length ($L_e = c/\omega_{pe} \lesssim 10^3$ km), and, therefore, are often extremely short compared with typical system scale lengths like the diameter of a planetary magnetosphere ($r_{\text{Magn.,Earth}} \approx 10^{5\ldots6}$ km), the solar radius ($r_\odot \approx 7 \times 10^5$ km), or an Astronomical Unit (1 AU $\approx 1.5 \times 10^{11}$ m), see, e.g., the reviews in Tsurutani and Stone [2].

Second, there is the numerical challenge to resolve narrow, potentially discontinuous, small-scale structures in extended systems with several (phase) space

* Corresponding author.
E-mail address: jk@tp4.ruhr-uni-bochum.de (J. Kleimann).

0010-4655/$ – see front matter
doi:10.1016/j.comphy.2003.12.003

dimensions without producing numerical artifacts like oscillations or even unphysical solutions (as, e.g., discussed by LeVeque [3] and LeVeque et al. [4]). Several numerical difficulties have been addressed with the development of special techniques. For example, the detailed treatment of extended, non-localized systems with a simultaneous resolution of internal small-scale structures can be achieved with *adaptive mesh refinement* (AMR), see, e.g., Friedel et al. [5] and Grauer et al. [6]. Oscillations can be suppressed with new numerical schemes like the *central weighted essentially non-oscillatory* (CWENO) algorithm proposed recently by Levy et al. [7,8] and Kurganov and Levy [9] for the numerical solution of systems of hyperbolic partial differential equations.

With the present study we report on an MHD-based evaluation of the first numerical scheme that combines the CWENO algorithm with a block-structured AMR technique.

In the following, we describe the physics contained in the newly developed code (Section 2) and the numerical approach taken to solve the relevant equations (Section 3). We report in detail about the code performance for a set of standard tests (Section 4), and we illustrate the application to the 'real world' problem of a Sedov explosion (Section 5). Finally, we conclude with a summary of the results and a brief discussion of prospective applications (Section 6).

2. Model equations

For the purpose of testing as well illustrating the computational approach discussed in the present paper, the numerical solution of the following set of nonlinear, normalized MHD equations is considered:

$$\partial_t \rho = -\nabla \cdot (\rho \mathbf{v}), \tag{1}$$

$$\partial_t (\rho \mathbf{v}) = -\nabla \cdot \left(\rho \mathbf{v}\mathbf{v} + (p + B^2/2)\mathbf{11} - \mathbf{B}\mathbf{B}\right), \tag{2}$$

$$\partial_t \mathbf{B} = -\nabla \cdot (\mathbf{v}\mathbf{B} - \mathbf{B}\mathbf{v}), \tag{3}$$

$$\partial_t e = -\nabla \cdot \left[(e + p + B^2/2)\mathbf{v} - (\mathbf{v} \cdot \mathbf{B})\mathbf{B}\right]. \tag{4}$$

These equations describe the time (t) evolution of an ideally conducting, quasi-neutral electron–proton plasma, considered as one fluid characterized by its mass density ρ, flow velocity $\mathbf{v}$, magnetic field $\mathbf{B}$, and polytropic index γ. The thermal pressure is given by $p = \rho\, T$ and the total energy density by

$$e = \frac{p}{\gamma - 1} + \frac{\rho v^2}{2} + \frac{B^2}{2}. \tag{5}$$

The symbol $\mathbf{11}$ in (2) is to be understood as $(\mathbf{11})_{ij} = \delta_{ij}$.

3. Numerical approach

3.1. The CWENO algorithm

The hyperbolic system of Eqs. (1) to (4) can be written in the form

$$\partial_t \mathbf{u} + \partial_{\mathbf{x}} f(\mathbf{u}) = \mathbf{Q}(\mathbf{x}, t, \mathbf{u}, \partial \mathbf{x}\mathbf{u}), \tag{6}$$

where the quantity $\mathbf{u} = \mathbf{u}(\mathbf{x}, t)$, the nonlinear convective flux $f = f(\mathbf{u})$ and the source term $\mathbf{Q}$ are vector-valued functions of the spatial vector $\mathbf{x}$ and time t. The basic idea is to separate the 'conservation law' part (equations with $\mathbf{Q} = \mathbf{0}$) from the sources.

During the last decade, significant progress has been made regarding the numerical solution of systems of hyperbolic conservation laws. Besides Riemann or approximate Riemann solvers [3], the promising concept of weighted essentially non-oscillatory (WENO) schemes, a review of which is given by Shu [10], has been developed. One of the latest improvements is a central WENO, or CWENO, introduced by Levy et al. [7,8]. The main advantage of the CWENO scheme is simplicity: one only has to know an estimate of the maximum propagation speeds of perturbations, and there is no need to solve a Riemann problem. We employ the CWENO technique and, therefore for completeness, proceed to describe the basic idea of a third-order, semi-discrete CWENO algorithm as it was proposed by Kurganov and Levy [9]. For simplicity of the argument, only the one-dimensional case is treated here. (Consequently, x and u denote one component of the vectors $\mathbf{x}$ and $\mathbf{u}$, not their lengths.)

To solve (6) for the case $Q = 0$ on a spatial grid of cell size Δx, the function u in each cell $I_j := [x_{j-1/2}, x_{j+1/2}]$ is approximated by a polynomial $P_j(x)$. This allows to define the cell average $\bar{u}_j^n$ (the lower horizontal lines in Fig. 1) of $u(x)$ at time $t = t^n := n\ \Delta t$ and position $x = x_{j+1/2} := (j + 1/2)\ \Delta x$

as

$$\bar{u}^n_{j+1/2} := \frac{1}{\Delta x}\left(\int_{x_j}^{x_{j+1/2}} P_j(x)\,\mathrm{d}x + \int_{x_{j+1/2}}^{x_{j+1}} P_{j+1}(x)\,\mathrm{d}x \right). \tag{7}$$

Sampling (6) at the cells $[x_j, x_{j+1}]$ and integrating from t^n to t^{n+1} then yields

$$\bar{u}^{n+1}_{j+1/2} = \bar{u}^n_{j+1/2} - \frac{1}{\Delta x} \int_{t^n}^{t^{n+1}} \big[f\big(u(x_{j+1},\tau)\big) - f\big(u(x_j,\tau)\big) \big]\,\mathrm{d}\tau. \tag{8}$$

The accuracy of $\bar{u}^{n+1}$ in (8) depends on the choice of the polynomials P_j and the method by which the integral is evaluated. The CWENO scheme uses for P_j a convex sum of two linear polynomials $P_{\mathrm{L},j}$ and $P_{\mathrm{R},j}$, and one parabola $P_{\mathrm{C},j}$ centered at x_j:

$$P_j(x) = \sum_{\alpha\in\{\mathrm{R,C,L}\}} g_\alpha P_{\alpha,j}(x) \tag{9}$$

with $\sum_\alpha g_\alpha = 1$ and $g_\alpha > 0$. $P_{\mathrm{C},j}$ is defined by

$$\sum_{\alpha\in\{\mathrm{R,C,L}\}} c_\alpha P_{\alpha,j}(x) = P_{\mathrm{exact},j}, \tag{10}$$

where $P_{\mathrm{L},j}$, $P_{\mathrm{R},j}$ and $P_{\mathrm{exact},j}$ reproduce the cell averages $(\bar{u}_{j-1}, \bar{u}_j)$, $(\bar{u}_j, \bar{u}_{j+1})$ and $(\bar{u}_{j-1}, \bar{u}_j, \bar{u}_{j+1})$, respectively. That is, $P_{\mathrm{R},j}(x_j) = \bar{u}_j$, $P_{\mathrm{R},j}(x_{j+1}) = \bar{u}_{j+1}$ and analogously for $P_{\mathrm{L},j}$ and $P_{\mathrm{exact},j}$. For a central scheme, the c_α are chosen symmetrically, e.g., $c_\mathrm{L} = c_\mathrm{R} = 1/4$, $c_\mathrm{C} = 1/2$, which can be shown to guarantee third-order accuracy.

Many other schemes tend to produce numerical artifacts (oscillations) at strong gradients. CWENO avoids this by checking the difference $(u^n_j - u^n_{j\pm1})$ to neighboring cells and by adjusting the weights g_j for the polynomial reconstruction such that the side which varies least provides the largest contribution to the construction of P_j, while in smooth regions, all components contribute equally. The polynomials are shown as bold curves in Fig. 1.

The polynomials obtained from the procedure described above are continuous within each cell but not across the cell boundaries. Consequently, there are discontinuities that propagate with characteristic velocities, like that of the fast mode in the MHD case. In order to estimate the location of these propagating discontinuities, we introduce an upper threshold a_j for their propagation velocity. Thus, the discontinuity lies within a triangular area in (x,t) space bounded by two lines $x = x_{j+1/2} \pm a_j(t - t^n)$, the so-called Riemann fan (wedge-shaped areas in Fig. 1). The time integration is now performed separately in both the smooth region and the Riemann fans by a standard numerical stepping scheme like Runge–Kutta. This leads to new cell averages $\overline{w}^{n+1}_j$ (smooth region) and $\overline{w}^{n+1}_{j+1/2}$ (Riemann fan). From these values we again reconstruct polynomials $\widetilde{w}^{n+1}_j$ and $\widetilde{w}^{n+1}_{j+1/2}$ with the above-mentioned algorithm. The cell-averages u^{n+1}_j on the original grid at the new time (upper part of Fig. 1) can now be computed from these three contributions with a formula similar to Eq. (8).

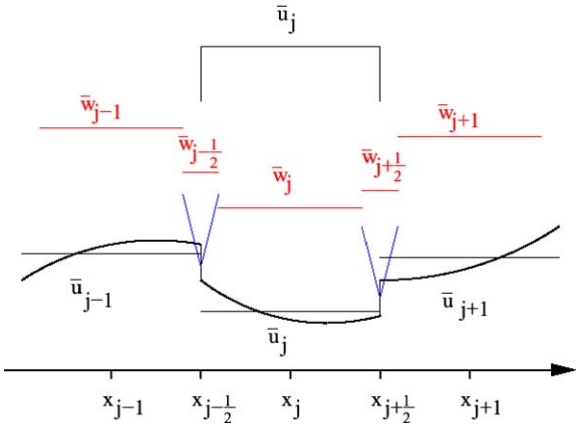

Fig. 1. CWENO differencing. The representation of u using cell polynomials (bold curves) causes discontinuities at the cell boundaries which propagate within the Riemann fans (wedge-shaped areas). Both grids, smooth and non-smooth, are integrated in time and then projected back onto the uniform grid. Adopted from Kurganov and Levy [9].

3.2. Adaptive mesh refinement

The idea of adaptive mesh refinement is near at hand. Starting with one grid of given resolution (in most of our three-dimensional configurations we currently chose $60 \times 60 \times 60$ mesh points), the MHD equations (1) to (4) are solved with the CWENO scheme as described above. After a certain number of time steps, it is checked whether the local numerical resolution is still sufficient on the entire grid. If finer grids are needed, a first local refinement is carried

out. In order to prepare for it, the points where the error of discretization exceeds a given value are marked. In addition to these grid points, adjacent ones are included. These marked points of insufficient numerical resolution have to be covered with rectangular grids of finer resolution as efficiently as possible. Our algorithm for this purpose is very similar to the one used by Berger and Colella [11], and was described in detail by Friedel et al. [5]. On the grids of the newly built level, the spatial discretization length and the time step are reduced by a factor of 2. The new grids are filled with data obtained by interpolation from the preceding coarser level. The integration advances on both levels until the resolution again becomes locally insufficient. The rebuilding of the grid hierarchy starting with the current level and proceeding on all subsequent levels begins when the above-mentioned error threshold is locally exceeded, e.g., if the regions of strong gradients have moved out of the region covered with finer grids, or if additional local gradients have developed, such that the prescribed accuracy is no longer guaranteed. The points of insufficient numerical resolution are collected on all grids of each level. On the basis of the resulting list, new grids are generated. After assuring that the latter are properly embedded in their parent grids, interpolated data are filled in. If data existed on grids of the same level before the regriding, these are used instead of the data interpolated from the parent grids.

The length of the time step is dynamically adapted to ensure that the Courant–Friedrich–Levy condition is met at all times.

The implementation of the adaptive mesh refinement strategy is done in C++. Handling of the data structures is separated from the problem under consideration. Therefore, it is relatively easy to use the code for other types of problems, like, e.g., the three-dimensional incompressible Euler equations [6]. We implemented the parallelization using POSIX threads, so that the code is actually portable but restricted to work on shared memory machines.

4. Numerical tests and performance evaluation

Since the publication of the now ‘classical’ paper by Sod [12] establishing the one-dimensional “shock tube” problem as a standard test for numerical schemes, an entire suite of one- and two-dimensional test cases has become available (see, e.g., Stone et al. [14]). While it appears that three-dimensional standards have not yet been developed to the same level, some can be constructed straightforwardly.

In this and the following section the potential of the new approach is demonstrated by discussing its performance for a number of test problems in one, two and three spatial dimensions (see, e.g., Fryxell et al. [13]).

4.1. The hydrodynamical advection problem

In order to see how the code handles flow problems in planar geometries, we consider the following reduced system of partial differential equations for density $\rho = \rho(x,t)$ and velocity $v = v(x,t)$

$$\partial_t \rho + \partial_x(\rho v) = 0, \tag{11}$$

$$\partial_t(\rho v) + \partial_x(\rho v^2) = 0, \tag{12}$$

which is obtained by substituting $p = 0$ and $B = 0$ into the one-dimensional version of our Eqs. (1) and (2). Subjected to the initial conditions

$$\rho(x,0) = \rho_0(x) \quad \text{and} \quad v(x,0) = v_0, \tag{13}$$

this so-called advection problem is easily shown to have

$$\rho(x,t) = \rho_0(x - v_0 t), \tag{14}$$

$$v(x,t) = v_0 \tag{15}$$

as analytical solution. The initial density profile is, thus, simply advected with constant fluid speed v_0 without changing its shape. Therefore, any deformation that *does* occur must be a numerical artifact. Advection test of this type were proposed by, e.g., Boris and Book [15]. Fig. 2 shows advection runs for different spatial resolutions using the box-shaped function

$$\rho_0(x) := \begin{cases} 1.2 & \text{if } |x| \leqslant 1/3, \\ 1.0 & \text{otherwise} \end{cases} \tag{16}$$

as initial profile. While the numerically caused asymmetric deformation of the density pulse is obvious, its comparatively large value of about 10 percent merely reflects the effect of numerical dissipation on the unphysically large gradient present at the steps. The ‘dissipation zone’ on the lower panel of Fig. 2 only spans a few grid cells and clearly diminishes in size

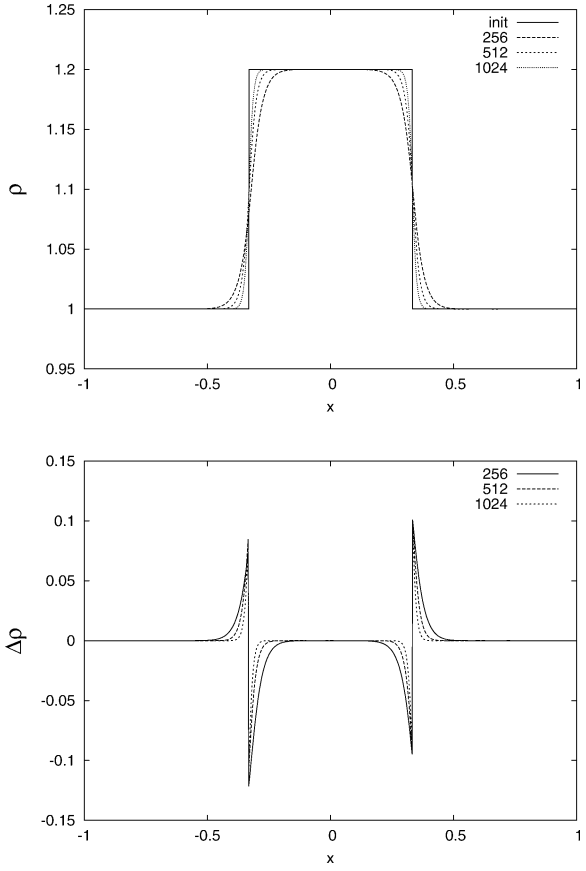

Fig. 2. Advection runs using (16) as initial profile and $v_0 = 0.5$ on the periodic domain $x \in [-1, 1]$. Upper panel: profiles at $t = 4$ (i.e. after one domain pass, dotted) for different values of spatial resolution (256, 512, and 1024 grid points) vs. their initial counterpart (16) (solid). Lower panel: Point-wise absolute deviation from the expected shape.

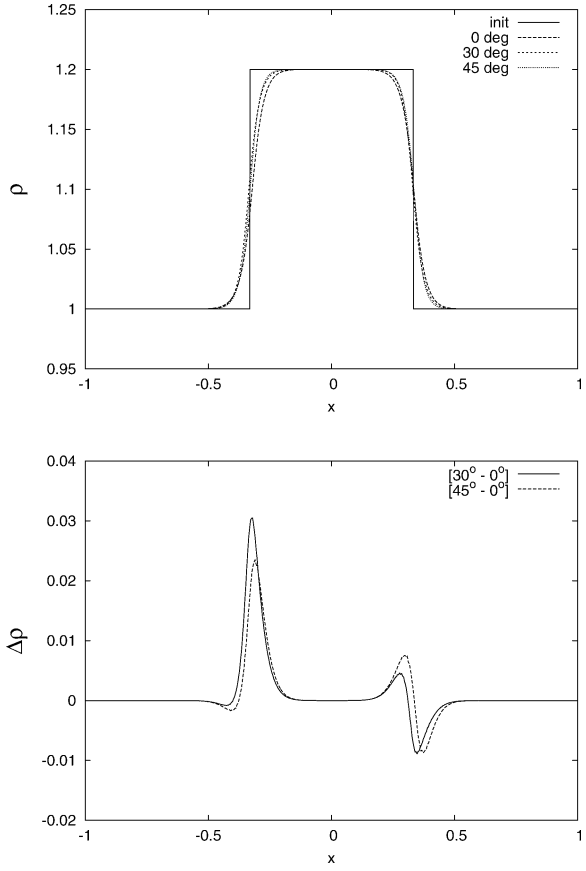

Fig. 3. Oblique advection runs at orientations $\vartheta \in \{0°, 30°, 45°\}$ using a mesh resolution which corresponds to 256 grid points in the direction of motion (e.g., $256/\cos\vartheta$ and $256/\sin\vartheta$ in x and y direction, respectively). Upper panel: density profiles after one domain pass. Below: absolute deviation of $\vartheta \in \{30°, 45°\}$ runs from the reference profile $\vartheta = 0°$. Parameters used are those of the parallel runs above.

with growing resolution. Note in particular the absence of oscillatory artifacts known from conventional schemes.

For the preceding computations, the direction of both v and the gradient of ρ were oriented parallel to the x-axis, such that for this truly one-dimensional setting, only a few grid points in the y- and z-direction were required for using the three-dimensionally coded CWENO scheme. However, since the results should be independent of our choice of coordinates, we also considered the above setting in an implementation were the system's plane of symmetry makes an angle $\vartheta \neq 0°$ with the x-axis. While the physical situation of course remains unchanged, the code no longer 'knows' about the symmetry of the problem. Nevertheless, the generated data must still correctly reproduce the expected profile in the rotated frame of reference. That this is indeed the case is demonstrated by the results displayed in Fig. 3. Evidently, the deviations due to the rotated frame of reference, and, thus, due to multi-dimensional modeling are within a few percent relative to each other. The smoothness of these plots should be attributed to the fact that these inclined cuts were produced by linear interpolation onto the rectangular grid. Note also that, while the settings of Figs. 2 and 3 describe the same physical problem, the underlying numerical problems, however, are quite

different: in the first case, the propagation is parallel to the grid, while it is inclined (and thus 2D) in the latter case. In the limit of infinitely small grid size, these discrepancies should of course disappear.

4.2. Shock tube problems

The 'shock tube' problem (Riemann problem) was first used by Sod [12] to examine a code's ability to handle strong gradients and to correctly reproduce the Rankine–Hugoniot jump conditions: two homogeneous domains of different gas pressures and densities are separated by a membrane. Being initially at rest in both domains, the fluid will develop various types of propagating discontinuities as soon as said membrane is removed. For the emerging time-dependent (but self-similar) profiles, semi-analytic solutions are known and may, thus, be used to evaluate the code's reliability for this important class of simulations.

We have investigated simulations using both Sod's original parameters as well as the 'strong shock tube' problem (see Fryxell et al. [13], Calder et al. [16]), which, due to its rather extreme choice of numbers, poses an even tougher test case. This purely hydrodynamic setting has been extended to include magnetic fields by Brio and Wu [17] in two fashions: The case with a field component (say, B_y) parallel to the shock plane (henceforth 'BW1') can be reduced to the purely hydrodynamic problem by simply substituting $p \to p + B_y^2/2$, while an additional perpendicular component $B_x = B_{x0} \neq 0$ no longer permits an analytic solution. (This case will be referred to as 'BW2' from here on). Table 1 summarizes the relevant initial conditions on both sides of the membrane.

Since, by construction, shock tube problems always feature both strong gradients and regions of uniform flow properties, they represent an ideal test case for our AMR algorithm. All runs presented below were done using an initial grid resolution of 128 points. The AMR routine was activated to identify the location of discontinuities and to subsequently double the resolution around them (multiple times if required), thus reaching an effective resolution of 1024 points. The panels of Figs. 4 and 5 illustrates the code's performance for this suite of standard shock tube problems. The quality of the results is evident when compared to those obtained by, e.g., LeVeque et al. [4], Calder et al. [16] and Ryu and Jones [18] for the standard, strong, and magnetic shock tube problem, respectively. Note that a grid refinement not only occurs at discontinuities in the solution curves, but also at locations of strong changes in their gradients.

5. Sedov explosion

The Sedov test case [19] of a spherical explosion into a homogeneous medium is well suited to test the symmetry properties of the code. All the initial energy of the explosion is deposited in a localized region around the origin. To be more specific, the localized region has a radius of size $\delta r = 0.01$, inside of which the pressure for the three-dimensional problem is given by

$$p_{\text{inside}} = \frac{3(\gamma - 1)}{4\pi(\delta r)^3}. \tag{17}$$

Outside this region the pressure is set constant to $p_{\text{outside}} = 10^{-5}$, while the density is set to $\rho = 1$ everywhere. The initial resolution was set to 64^3 mesh points with two levels of refinement, corresponding to an effective resolution of 256^3 mesh points. Although the resulting fronts of the developing (self-similar) blast wave (see Fig. 7) are very steep, their profiles are sharp and completely void of any oscillatory artifacts. Note also that the code retains the problem's radial symmetry with respect to the origin.

Table 1
Values of density, pressure, magnetic field, and adiabatic exponent γ for the shock tube simulation

	ρ_{left}	ρ_{right}	p_{left}	p_{right}	$B_{y,\text{left}}$	$B_{y,\text{right}}$	B_x	γ
Standard	1	0.125	1	0.1	–	–	–	1.4
Strong shock	10	1	100	1	–	–	–	1.4
BW 1	1	0.125	1000	0.1	1	−1	–	2
BW 2	1	0.125	1000	0.1	1	−1	0.75	2

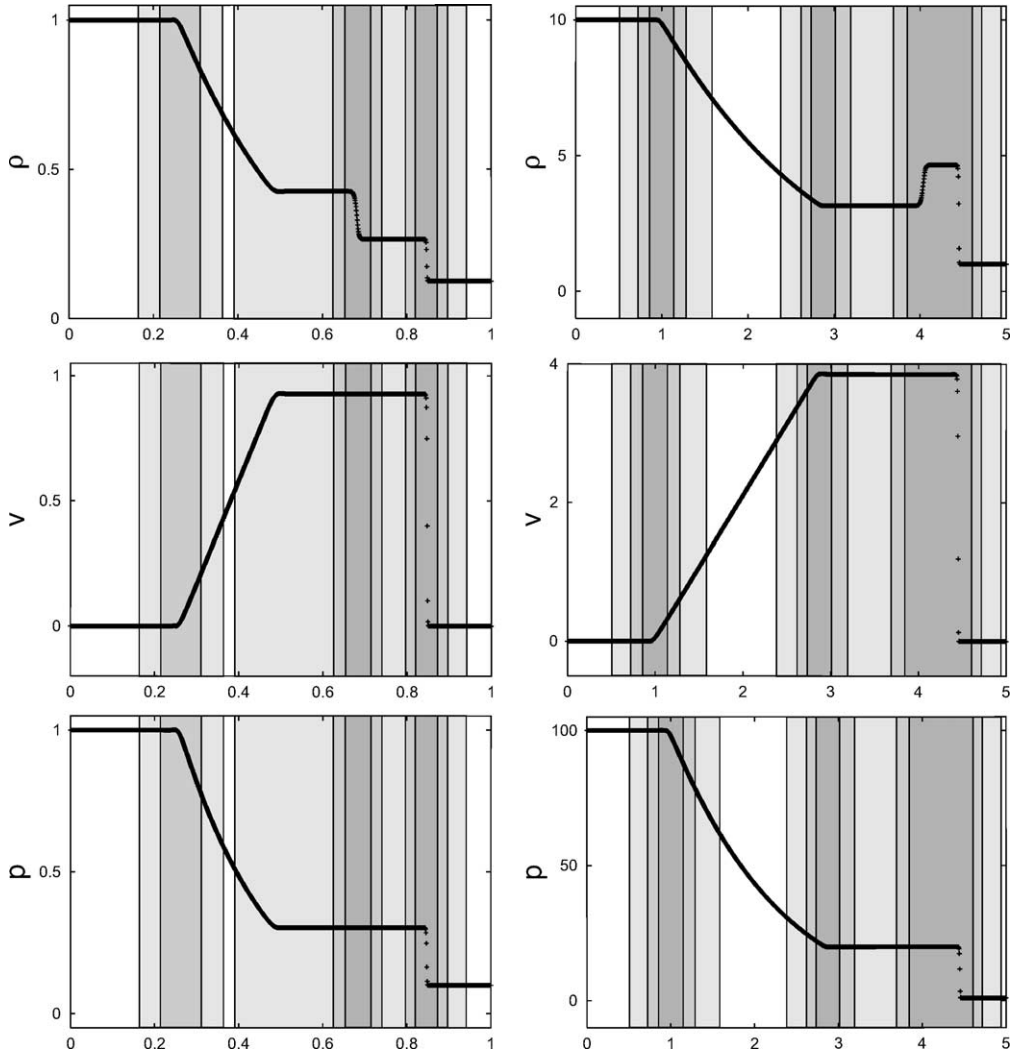

Fig. 4. Profiles of density (upper panel), velocity (middle panel), and gas pressure (lower panel) for both the standard shock tube problem at time $t = 0.2$ (left) and for the strong shock tube problem at $t = 0.4$ (right). Shading indicates the sections at which the initial resolution was refined by a factor of two, four, and eight, respectively.

The computational process which defines the location of refinement areas will generally result in an asymmetric distribution of blocks, even if the underlying physical problem is void of any such asymmetries. (For a detailed description of the regriding algorithm see Friedel et al. [5].) Therefore, a planar cut through the computational domain (as shown on the left panel of Fig. 7) cannot capture the full block structure information. The 3D rendering of Fig. 6 may thus serve as a better illustration of the refinement process.

6. Summary and outlook

A new code for the time-dependent modeling of 3D MHD problems is presented. In order to improve, in particular, the study of plasma discontinuities, the code is developed as a numerical realization of the so-called CWENO scheme combined with the concept of adaptive mesh refinement. While the first is a powerful state-of-the-art attempt to suppress unphysical oscillations when computing discontinuities, the

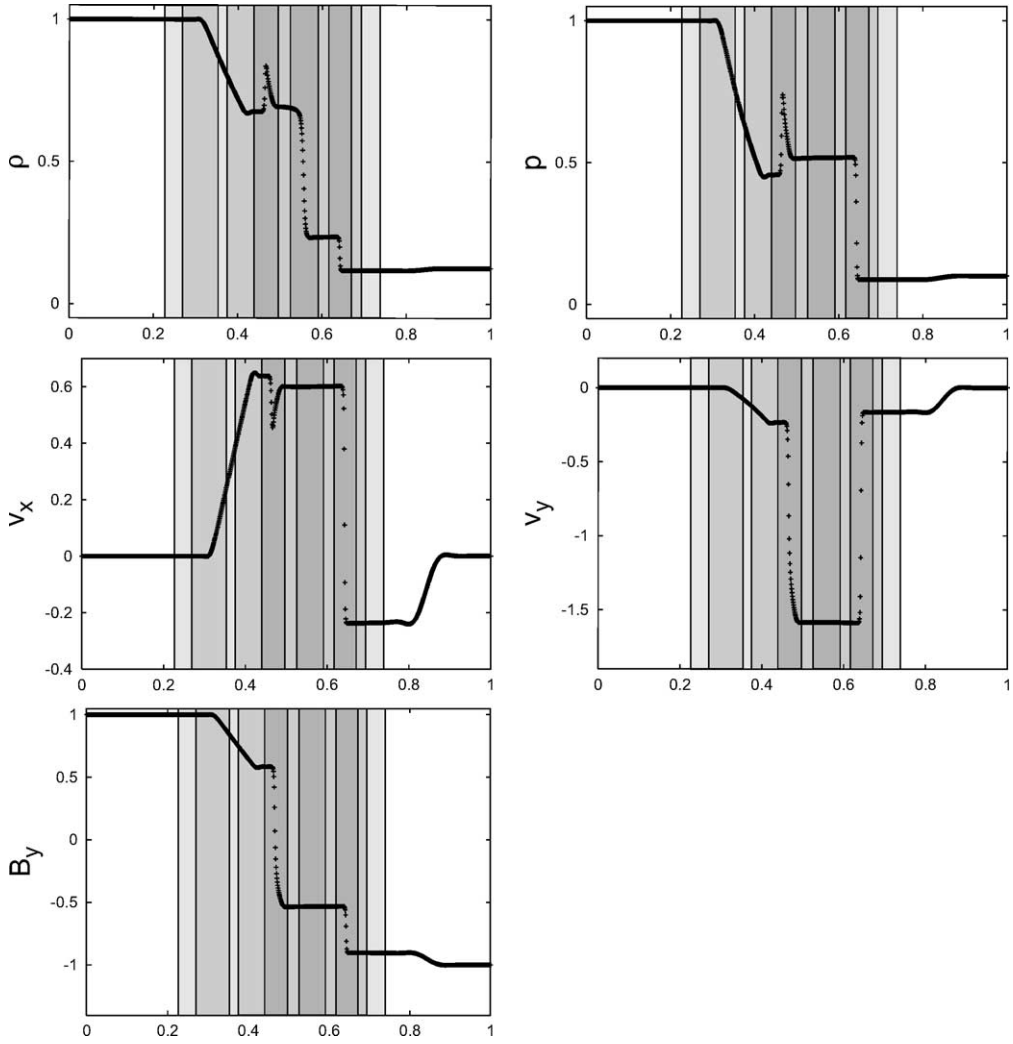

Fig. 5. Profiles of density, gas pressure, and velocity for the MHD shock tube problem 'BW2' at time $t = 0.1$. In addition to the previous panels, the v and B field component parallel to the shock plane are shown. The perpendicular magnetic field component B_x stays equal to its initial, constant value (not shown here).

second provides for high resolution of the latter. Both achievements are desirable prerequisites for a refined investigation of plasma discontinuities, particularly for shocks in space plasmas. The knowledge of the detailed structure of such shocks is, for example, required for an insightful comparison with data and is important for an understanding of particle acceleration.

The present paper serves to describe the new code and to demonstrate its reliability by applying it to a set of standard test problems (pulse advection, shock tubes, Sedov explosion) in one, two and three space dimensions. The numerical solution of these problems indicate the potential of the CWENO-based approach to model time-dependent, multi-dimensional MHD problems requiring high spatial resolution.

With forthcoming work, we intend to employ the new tool for a study of structures in space plasmas, which are increasingly gaining interest in the context

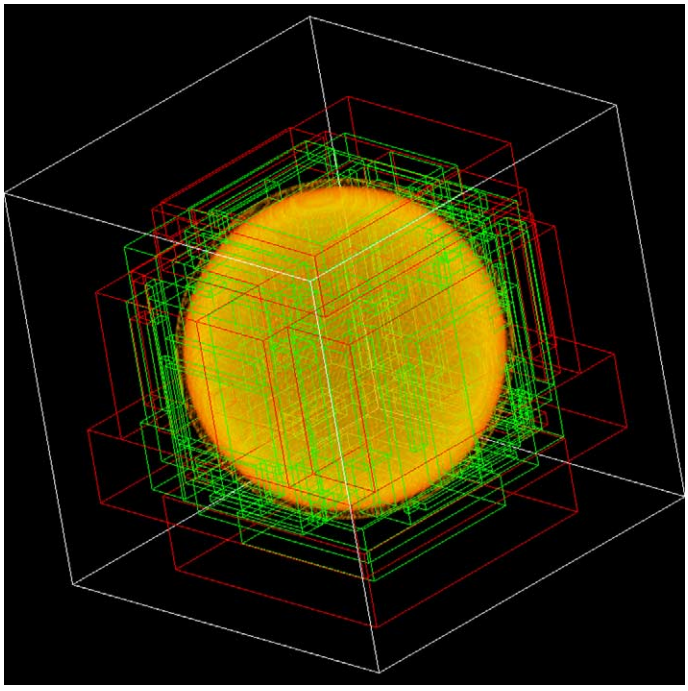

Fig. 6. Volume rendering of the energy distribution of a Sedov explosion at time 0.05, showing also covering with adaptive meshes from two levels of refinement.

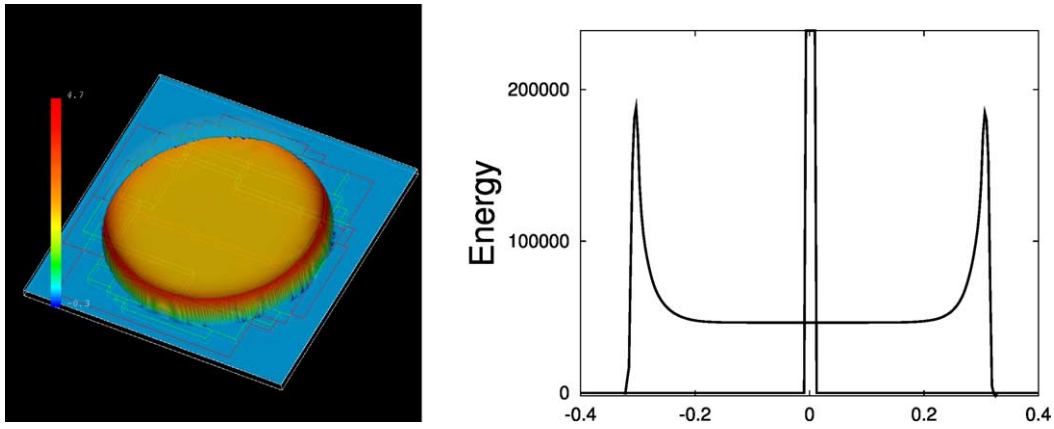

Fig. 7. Left: Plane cut through the origin showing the energy distribution at time 0.05 as a surface plot, again with refined areas superimposed. Right: One-dimensional cut though the origin showing energy density at time $t = 0.05$ (scaled by a factor 10^4) and $t = 0$.

of space weather, i.e. the time-varying plasma conditions in the Earth vicinity. The results of a first step along this line of modeling, namely a simple model of an eruptive disturbance leaving the Sun, have already been presented in Kleimann et al. [20].

Acknowledgements

This work benefited of support from INTAS contract 00-292. Computational resources were provided by *Hewlett Packard* in the framework of their *Itanium*

Award. Furthermore, we gratefully acknowledge financial support by the *Wernher von Braun Foundation*.

References

[1] D. Biskamp, Magnetic Reconnection in Plasmas, in: Cambridge Monographs on Plasma Physics, Cambridge University Press, 2000.
[2] B.T. Tsurutani, R.G. Stone (Eds.), Collisionless Shocks in the Heliosphere, I and II, Geophysical Monograph, vol. 35, American Geophysical Union, 1985.
[3] R.J. LeVeque, Numerical methods for conservation laws, in: Lectures in Mathematics, Springer, Berlin, 1992.
[4] R.J. LeVeque, D. Mihalas, E.A. Dorfi, E. Müller (Eds.), Computational Methods for Astrophysical Fluid Flow, Saas-Fee Advanced Course 27, Lecture Notes, Swiss Society for Astrophysics and Astronomy, Springer, Berlin, 1997.
[5] H. Friedel, R. Grauer, C. Marliani, J. Comput. Phys. 134 (1997) 190.
[6] R. Grauer, C. Marliani, K. Germaschewski, Phys. Rev. Lett. 80 (1998) 4177.
[7] D. Levy, G. Puppo, G. Russo, Math. Model. Numer. Anal. 33 (2000) 547.
[8] D. Levy, G. Puppo, G. Russo, SIAM J. Sci. Comput. 22 (2000) 656.
[9] A. Kurganov, D. Levy, SIAM J. Sci. Comput. 22 (2000) 1461.
[10] C.-W. Shu, Advanced numerical approximation of nonlinear hyperbolic equations, in: A. Quarteroni (Ed.), Lecture Notes in Mathematics, Springer, Berlin, 1998, p. 325.
[11] M.J. Berger, P. Colella, J. Comput. Phys. 82 (1989) 64.
[12] G. Sod, J. Comput. Phys. 27 (1978) 1.
[13] B. Fryxell, et al., Astrophys. J. (Suppl. Ser.) 131 (2000) 273.
[14] J.M. Stone, J.F. Hawley, C.R. Evans, M.L. Norman, Astrophys. J. 388 (1992) 415.
[15] J.C. Boris, D.L. Book, J. Comput. Phys. 11 (1973) 38.
[16] C.A. Calder, et al., Astrophys. J. (Suppl. Ser.) 229 (2002) 143.
[17] M. Brio, C.C. Wu, J. Comput. Phys. 75 (1988) 400.
[18] R. Ryul, T.W. Jones, Astrophys. J. 442 (1995) 228.
[19] L.I. Sedov, Similarity and Dimensional Methods in Mechanics, Academic Press, New York, 1959.
[20] J. Kleimann, H. Fichtner, A. Kopp, R. Grauer, K. Germaschewski, Proc. 10th Europ. Solar Phys. Meeting 1 (2002) 21.